© 2020. Published by The Company of Biologists Ltd | Development (2020) 147, dev187633. doi:10.1242/dev.187633

TECHNIQUES AND RESOURCES

RESEARCH ARTICLE

The visible skeleton 2.0: phenotyping of cartilage and bone in fixed vertebrate embryos and foetuses based on X-ray microCT

Simone Gabner[1], Peter Böck[1], Dieter Fink[2], Martin Glösmann[3] and Stephan Handschuh[3,*]

ABSTRACT

For decades, clearing and staining with Alcian Blue and Alizarin Red has been the gold standard to image vertebrate skeletal development. Here, we present an alternate approach to visualise bone and cartilage based on X-ray microCT imaging, which allows the collection of genuine 3D data of the entire developing skeleton at micron resolution. Our novel protocol is based on ethanol fixation and staining with Ruthenium Red, and efficiently contrasts cartilage matrix, as demonstrated in whole E16.5 mouse foetuses and limbs of E14 chicken embryos. Bone mineral is well preserved during staining, thus the entire embryonic skeleton can be imaged at high contrast. Differences in X-ray attenuation of ruthenium and calcium enable the spectral separation of cartilage matrix and bone by dual energy microCT (microDECT). Clearing of specimens is not required. The protocol is simple and reproducible. We demonstrate that cartilage contrast in E16.5 mouse foetuses is adequate for fast visual phenotyping. Morphometric skeletal parameters are easily extracted. We consider the presented workflow to be a powerful and versatile extension to the toolkit currently available for qualitative and quantitative phenotyping of vertebrate skeletal development.

KEY WORDS: Ruthenium Red, Contrast agent, Cartilage staining, Skeletal development, Dual energy CT, µCT

INTRODUCTION

The study of skeletal development has intrigued biologists for more than a century and facilitated our understanding of developmental networks and vertebrate evolution. Today, skeletal imaging is as relevant as ever, aiding in the characterisation of animal models and developmental malformations (see e.g. Bird et al., 2018; Lecanda et al., 2000; Li et al., 1999; White et al., 2003). Skeletal development in vertebrate model species such as zebrafish, *Xenopus*, chicken and mouse is classically visualised by clearing and staining, a technique in which cartilage and bone is labelled with Alcian Blue and Alizarin Red, respectively, whereas non-skeletal tissue is rendered transparent by clearing (Dingerkus and Uhler, 1977; Hanken and Wassersug, 1981; Park and Kim, 1984; Shapiro, 1992; Simons and van Horn, 1971; Wassersug, 1976). In 1981, Hanken and Wassersug demonstrated the wide applicability of clearing and staining in their seminal paper 'The Visible Skeleton', and, ever since, this technique has been key in studying whole-embryo skeletal development. Cleared and stained embryos provide great anatomic detail. However, specimens are mostly documented in 2D and therefore limited in information. Arguably, quantitative and geometrically isotropic 3D data of the developing skeleton would provide more complete datasets, further fostering our understanding of vertebrate development. So far, a number of studies have successfully imaged Alcian Blue stained cartilage in 3D in cleared specimens using optical projection tomography (OPT) (Capellini et al., 2011; Chandaria et al., 2016; Pardo-Martin et al., 2013). Other approaches to 3D imaging of cartilage development include immunohistochemical labelling of collagen type II in small specimens for confocal laser scanning microscopy (Brunt et al., 2015; Lukas and Olsson, 2018) or microscopic X-ray computed tomography (microCT) imaging (Metscher and Müller, 2011), 3D phase-contrast X-ray tomography or magnetic resonance imaging of larger foetuses (Okumura et al., 2017), high-resolution episcopic microscopy (Reissig et al., 2019), and cartilage visualisation based on manual segmentation of serial sections (Yaryhin and Werneburg, 2019) and microCT volumes (Kaucka et al., 2018). Likewise, developing bone has been imaged in 3D mainly using microCT (Oest et al., 2008), but also using other approaches such as confocal microscopy of Alizarin Red stained specimens (Sakata-Haga et al., 2018) or two-photon microscopy (Jing et al., 2018). Novel clearing protocols for hard tissues (see, for example, Greenbaum et al., 2017) will further improve light-optical 3D imaging of skeletal development; however, so far no workflow has been reported that allows simultaneous isotropic 3D imaging of bone and cartilage with similar quality, to allow the reliable separation and intensity-based visualisation of both skeletal tissues.

Among the microscopic 3D imaging techniques in the life sciences, microCT recently gained in importance as it provides genuine isotropic 3D images of fixed non-transparent biological probes at micron resolution. For more than a decade, it has been routinely used for quantitative imaging of mineralised tissue in adult animal models (Bouxsein et al., 2010) and bone development (Oest et al., 2008; Solomon et al., 2018). With the introduction of X-ray dense contrast agents, microCT enabled high-contrast soft-tissue imaging (Johnson et al., 2006; Metscher, 2009; Mizutani and Suzuki, 2012), and has proven to be suitable for high-throughput embryo phenotyping (Adams et al., 2013; Dickinson et al., 2016; Wong et al., 2012, 2014). Most recently, protocols allowing the specific labelling of cellular components, such as cytoplasm (Busse et al., 2018) or cell nuclei (Müller et al., 2018), have become available, gradually paving the way towards a three-dimensional and isotropic virtual histology based on microscopic X-ray images.

In order to move the concept of clearing and staining to isotropic 3D image volumes based on X-ray microCT, the key step is selective labelling of cartilage matrix, while bone mineral is readily visible based on its intrinsic X-ray density. So far, several contrast agents have been used to increase X-ray contrast of hyaline cartilage

[1]Histology and Embryology, Department for Pathobiology, University of Veterinary Medicine Vienna, Veterinärplatz 1, A-1210 Vienna, Austria. [2]Institute of Laboratory Animal Science, University of Veterinary Medicine Vienna, Veterinärplatz 1, A-1210 Vienna, Austria. [3]VetCore Facility for Research/Imaging Unit, University of Veterinary Medicine Vienna, Veterinärplatz 1, A-1210 Vienna, Austria.

*Author for correspondence (stephan.handschuh@vetmeduni.ac.at)

S.H., 0000-0002-2140-7892

Handling Editor: James Briscoe
Received 18 January 2020; Accepted 23 April 2020

Development (2020) 147, dev187633. doi:10.1242/dev.187633

(including articular cartilage) using compounds containing gadolinium, iodine or tungsten (Cockman et al., 2006; Kerckhofs et al., 2013; Nieminen et al., 2015; Xie et al., 2010). Although these studies demonstrated that the quantitative assessment of proteoglycan and collagen distribution in articular cartilage is possible in osteoarthritis studies, none of these staining protocols is specific to cartilage matrix, i.e. published protocols for contrasting cartilage also stain other tissues in vertebrate embryos, at intensities possibly equal or higher to cartilage contrast.

Thus, the present study had the goal of developing an analogue of the clearing and staining technique for isotropic 3D imaging of bone and cartilage in fixed vertebrate embryos based on microscopic X-ray microCT. This includes three main aims: (1) to develop a protocol for labelling cartilage matrix with an X-ray dense contrast agent that provides sufficient contrast over other tissues to allow for automated visualisation and intensity-based segmentation of cartilage, making it a proper tool for quantitative high-throughput analysis of cartilaginous structures; (ii) to design this staining protocol in a way that leaves bone mineral unaffected, to enable the simultaneous imaging of the complete developing skeleton; this is crucial, as decalcification has been a common issue in clearing and staining protocols in the past (Yamazaki et al., 2011); (iii) to set up a microscopic dual energy CT (Handschuh et al., 2017; Martins de Souza E Silva et al., 2017) imaging protocol that would allow the spectral separation of cartilage and bone based on the different X-ray attenuation properties of bone mineral (hydroxyapatite) and the contrast agent for cartilage when imaging the specimen at different X-ray energy spectra, fostering comprehensive qualitative and quantitative evaluation.

RESULTS

In search of a suitable protocol, we screened several fixatives, washing agents and staining solutions. Before testing staining protocols on mouse foetuses, we performed preliminary staining experiments involving nine different fixatives and 11 different contrast agents. We finally ended up with a staining protocol that uses Ruthenium Red in 50% ethanol for labelling of cartilage matrix in ethanol-fixed samples. The Results section is dedicated to the detailed description of the optimised staining and imaging protocols; technical issues concerning fixation, washing and staining are addressed in the Discussion.

Ruthenium Red staining of E16.5 mouse foetuses

Staining with Ruthenium Red turned the E16.5 mouse foetuses dark purple (Fig. 1B,C). Inspection of the staining pattern on a cross-section of the foetus using a stereomicroscope revealed that all tissue except fat bound some Ruthenium Red (Fig. 1E). Soft tissues appeared pinkish under strong reflected light, while cartilage matrix

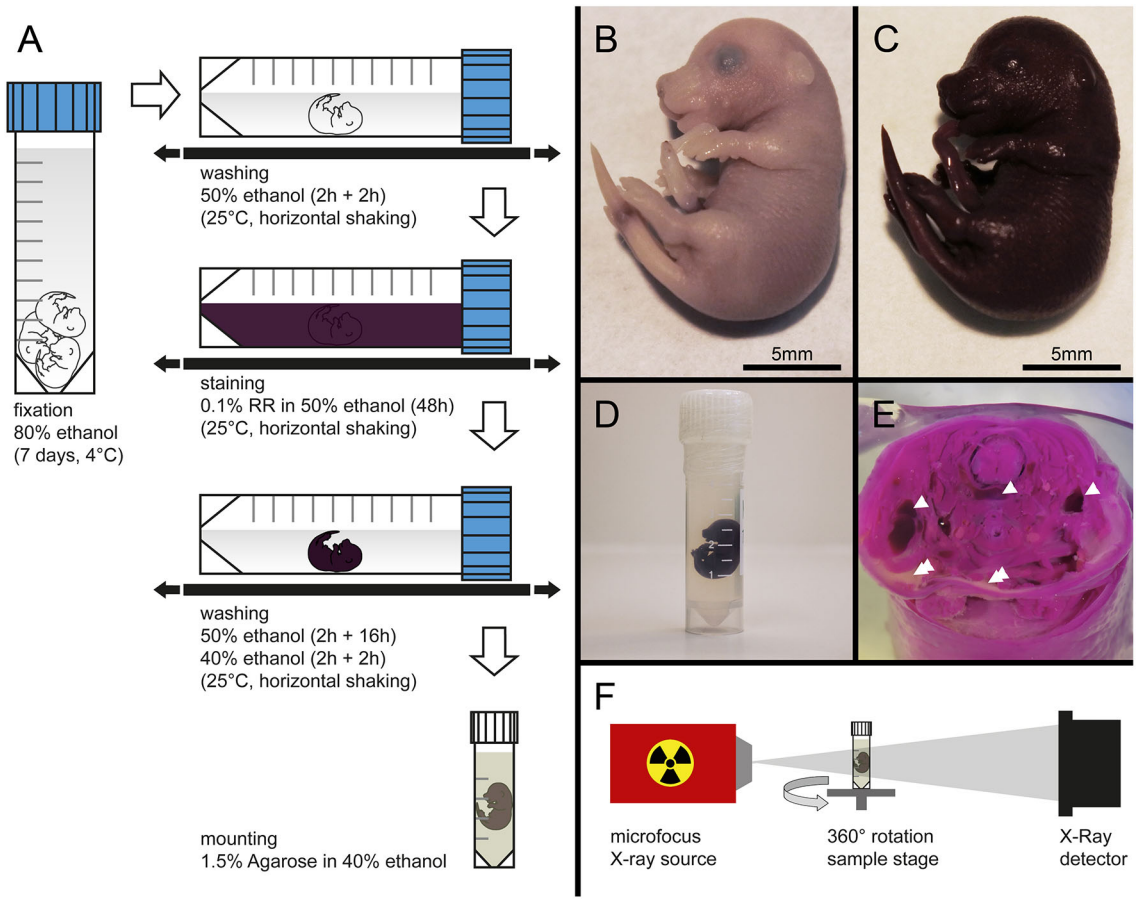

Fig. 1. Workflow for the preparation and subsequent microCT imaging of the specimens. (A) E16.5 mouse foetuses were fixed in 80% ethanol, partially rehydrated and stained in 0.1% (w/v) Ruthenium Red in 50% ethanol. (B) E16.5 mouse foetus after fixation. (C) The same foetus after Ruthenium Red staining. No apparent shrinkage of the embryo occurred during staining. (D) A foetus mounted for scanning in 1.5% low melt agarose. (E) A foetus cut in half after scan-acquisition and covered with a drop of water and a coverslip. Cross-sectional view of the foetus at height of the forelimb. Note the different binding of Ruthenium Red to different tissues. All soft tissue except fat (double arrowheads) bound Ruthenium Red, thus appearing pinkish. Cartilage retained Ruthenium Red the most, appearing dark purple (arrowheads). (F) Scheme of the X-ray imaging setup.

Development (2020) 147, dev187633. doi:10.1242/dev.187633

stained dark red/purple (Fig. 1E). Overall, Ruthenium Red staining under the employed conditions resulted in a relatively low total X-ray attenuation in the foetus in projection images (Fig. 2A) but still yielded reasonable contrast for cartilage matrix in reconstructed virtual slices (Fig. 2B,C, Movie 1). Mean Hounsfield units (CT numbers) of five representative soft tissues/inner organs, five cartilage elements and five bones are summarised in Table 1. While after Ruthenium Red staining soft tissues showed comparatively low X-ray attenuation when imaged at 60 kVp (soft tissue window: 100-400 HU, Fig. 3A, Movie 2), cartilage matrix showed up with higher CT numbers (cartilage window: 400-900 HU, Fig. 3B, Movie 3). This difference allowed the visualisation of the entire foetal skeleton by 3D volume rendering using the cartilage window (Fig. 3E, Movie 4). Alternatively, volume rendering depicted the entire foetus when using the soft tissue window (Fig. 3D, Movie 5). Bone showed generally higher CT numbers than stained cartilage (bone window: 900-2000 HU, Fig. 3C,F, Movies 6, 7). However, some bone segments (perhaps owing to little mineralisation or partial volume effects for very thin bones) yielded CT numbers below 900 HU and thus were not displayed in the bone window. These bone areas below 900 HU partly overlapped with intensity values observed in strongly stained cartilage matrix.

Information gained from microCT scans of skeletal development

Scans of entire E16.5 mouse foetuses (voxel resolution 8.77 µm) provided exquisite anatomic detail of skeletal elements, which could be readily used to display morphological features of e.g. the skull (Fig. 4A-B, Movies 8, 9), the limbs (Fig. 4C-F, Movies 10, 11) and the ribcage (Fig. 4H,I, Movie 12). In particular, limbs and ribcage are frequently evaluated in the context of developmental disorders and skeletal malformations. In the skull, the 60 kVp scans allowed the visualisation of the intricate spatial relationship between bone and cartilage [e.g. Meckel's cartilage and dentary (Fig. 4A), trabecular cartilage and vomer (Fig. 4B)] as well as ossification centres such as basioccipital and basisphenoid in the cranial base (Fig. 4B). Depiction of the hind limb (Fig. 4C,D) and the forelimb (Fig. 4E) revealed ossification centres in the pelvic and pectoral girdle, as well as in long bones of stylo- and zeugopodium, and also allowed the evaluation of minute skeletal elements of the autopodium. In the long bones of the limbs, dark zones can be distinguished between the ossification centres and the Ruthenium Red stained cartilage (Fig. 4C-F), which represent the hypertrophic cartilage zones containing more voluminous chondrocytes and less cartilage matrix, compared with the immature cartilage in epiphyses (for histological comparison, see Figs S1 and S2). In the ribcage, we confirmed the presence of 13 ribs as typical for laboratory mice, seven of which were connected to the cartilaginous sternum (Fig. 4H). All ribs were partly ossified and partly cartilaginous. The obtained microCT data further enormously facilitated the semi-automated quantitative analysis of standard morphometric measures. We showcase possible morphometric measurements in the forelimb and ribcage, demonstrating that volume and length of skeletal elements, such as humerus, radius, ulna (Fig. 4F) and rib 6 (Fig. 4I), can be easily extracted, providing valuable quantitative information on developmental processes.

Separation of bone and cartilage based on microscopic dual energy CT (microDECT)

As demonstrated above, foetal bone and cartilage overlapped in their X-ray attenuation, particularly between 700 and 900 HU, which were typical CT numbers for both strongly stained cartilage (e.g. in humerus and femur epiphysis) and foetal bone with low mineralization, rendering the different tissues indistinguishable. Therefore, we sought to establish a dual energy protocol to reliably separate cartilage from bone based on the different X-ray attenuation properties of hydroxyapatite and ruthenium at the two respective energy spectra. As we show, this was possible using a 40 kVp

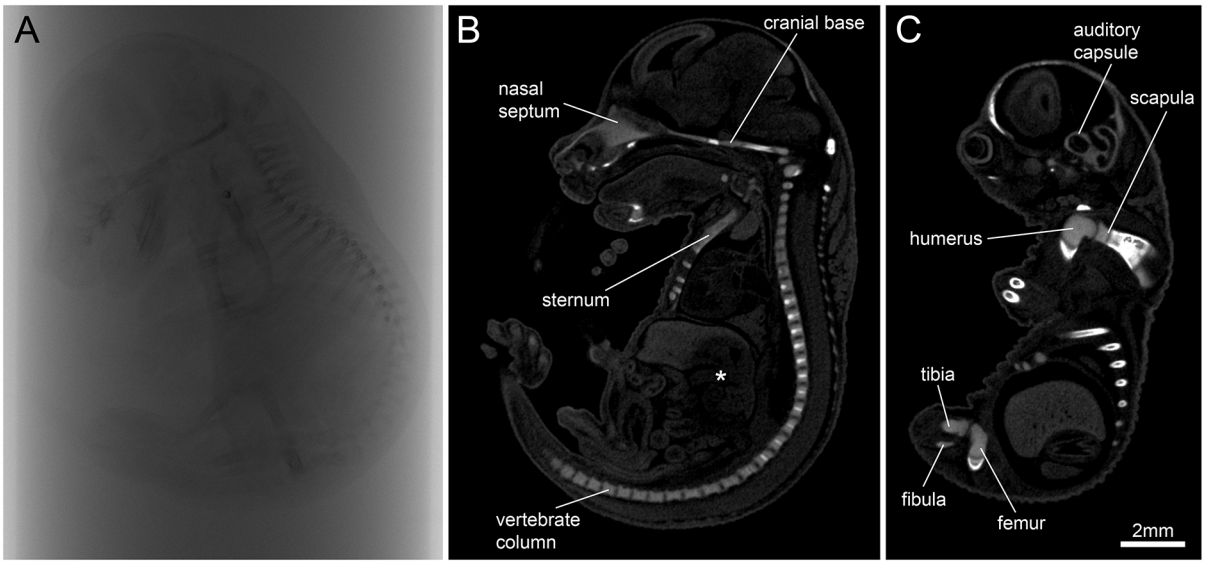

Fig. 2. MicroCT image acquisition and reconstructed virtual slices of an E16.5 mouse foetus stained with Ruthenium Red. A X-ray projection image of a Ruthenium Red stained and agarose-embedded mouse foetus acquired at 60 kVp/133 µA. The total X-ray attenuation in the sample was comparatively low. (B) Reconstructed midsagittal virtual slice of the same scan. Although soft tissues and internal organs, such as the brain, liver, heart and alimentary canal, could clearly be distinguished based on the staining background (see also Fig. 1E), cartilage matrix showed even higher image intensity values as can be seen, for example, in the sternum and vertebrate column. The centre of the liver (asterisk) did not take up as much Ruthenium Red stain as the outer regions of the liver, which potentially related to inadequate fixation of the specimen centre by the 80% ethanol fixative. (C) Parasagittal section of the same scan, showing the auditory capsule housing the semicircular canals, as well as joints between scapula/humerus and femur/tibia.

Development (2020) 147, dev187633. doi:10.1242/dev.187633

Table 1. Image intensity measurements taken from five selected soft tissues/inner organs, five cartilage elements and five bones

		Mean CT number (HU)	s.d. of CT number (HU)
Soft tissues and inner organs	Lung	190.68	39.12
	Eye	223.39	123.32
	Kidney	151.50	48.02
	Liver	251.28	41.89
	Heart	82.41	42.47
Cartilage	Humerus epiphyses	654.46	74.27
	Femur epiphyses	621.99	71.95
	Sternum	534.95	126.80
	Vertebrae	450.49	63.86
	Cranial base	404.47	61.64
Bone	Dentary	1269.42	342.11
	Humerus diaphysis	1278.94	412.66
	Femur diaphysis	1166.82	266.07
	Frontal	1234.81	312.83
	Scapula diaphysis	1225.66	328.22

Measurements show that cartilage matrix has generally higher mean CT numbers compared with soft tissues, but lower CT numbers compared with bone. Dermal (dentary, frontal) and endochondral (humerus, femur, and scapula) ossification sites show similar CT numbers. Cartilage CT numbers in the epiphyses of humerus and femur were higher compared with the vertebral centra, cranial base and sternum. Measurements represent pooled data (average mean, average s.d.) from three foetuses imaged at 60 kVp/133 µA.

(0.1 mm Mo filter)/60 kVp (Zeiss LE#2 filter) microDECT imaging protocol. Different spectral properties could already be seen in the 40 kVp/60 kVp overlay image (Fig. 3G), while extracted material fractions provided well-separated hydroxyapatite and ruthenium signals (Fig. 3H, Movie 13; for both image and movie, the histogram of the ruthenium material fraction was clipped to discard soft tissue and show only cartilage). We used these material fractions to create 3D volume renderings that closely mimic the appearance of specimens cleared and stained with Alcian Blue/Alizarin Red (Fig. 3I, Movie 14), but now provide genuine isotropic 3D information about the foetal skeleton and thus can be used for precise morphometric measurements. Based on microDECT datasets, the ossification of skeletal elements, such as long bones of the limbs (Fig. 4G, Movie 15) and bones of the axial skeleton (Fig. 4J, Movie 16), can be unambiguously evaluated, including the analysis of minute primary ossification centres such as those found in vertebral centra.

Imaging of E14 chicken embryo forelimbs

To show that the present protocol also works for other model species, we stained the forelimb (wing) of an E14 chicken embryo for 72 h with Ruthenium Red and imaged it with the same 60 kVp imaging protocol used previously on mice. For comparison, the contralateral wing was scanned without staining. Fig. 5 and Movie 17 demonstrate that staining for 72 h was sufficient to stain all cartilage in the E14 chicken forelimb. Comparison of stained and unstained forelimbs revealed minute elements of the autopodium that showed no ossification centre at this stage of development.

DISCUSSION

General merits of the presented workflow and comparison with traditional clearing and staining

With the presented workflow, we provide a novel tool for the 3D analysis of cartilage development in fixed vertebrate embryos and foetuses based on isotropic microCT datasets. So far, several contrast agents have been successfully employed for the qualitative and quantitative assessment of cartilage matrix by microCT. This includes negatively charged metal salts [e.g. phosphotungstic acid (Das Neves Borges et al., 2014; Karhula et al., 2017; Nieminen et al., 2015) and phosphomolybdic acid (Nieminen et al., 2015)] to image collagen, as well as positively charged compounds [e.g. gadolinium chloride (Cockman et al., 2006) and ioxaglate/Hexabrix (Kerckhofs et al., 2013; Xie et al., 2010; Xie et al., 2009)] to image proteoglycans. For a summary of contrast agents used for cartilage imaging, see de Bournonville et al. (2019). Most of these studies were carried out on extracted skeletal elements, and none of the published protocols proved to provide sufficient contrast of cartilage matrix against soft tissue for intensity-based visualisation or segmentation in intact embryos or animals. Thus, previous microCT studies addressing the phenotypic analysis of cartilage in intact embryos relied on time-consuming manual segmentation (see, for example, Kaucka et al., 2018). We provide here, for the first time, a high-contrast staining protocol allowing both visual phenotyping and intensity-based segmentation of cartilage elements, which can be used for qualitative and quantitative analysis of cartilage development (Fig. 4). The protocol separates cartilage matrix from most soft tissues and organs, with only the eye and hair follicles of vibrissae showing minor intensity overlaps with stained cartilage matrix (Fig. 4A,B).

Cleared and stained specimens provide excellent anatomical detail; however, they are usually documented in 2D. In comparison with images taken from cleared and Alcian Blue/Alizarin Red stained specimens, our workflow provides several advantages. (1) We provide genuine 3D information that may be used for quantitative morphometric analysis of cartilage and bone development. In addition to skeletal elements, our workflow also allows the analysis of soft tissues *in situ* (Fig. 2), thus enabling the simultaneous phenotyping of the skeleton and organs such as heart or brain. (2) Using microDECT (Figs 3 and 4), we demonstrate that two-channel imaging of the developing skeleton with lab-based instrumentation is feasible. Traditionally, the main disadvantage of X-ray compared with optical imaging was the limitation to grayscale image information. MicroDECT eliminates this old limitation and provides for the first time coloured 3D X-Ray images of the foetal mouse skeleton. (3) Imaging and quantitative morphometric analyses can potentially be fully automated in the future. (4) We generate digital 3D datasets (virtual embryos and foetuses) that may be shared and made publicly available in online data repositories.

Key findings in developing the presented staining protocol

This section briefly summarises key findings we have achieved from tests of other fixatives, contrast agents and washing solutions, to provide more detailed background information on the staining mechanism and insights into protocols that did not work.

Fixation

According to our findings, fixation is one of the key steps in the protocol. In the first step, we tested three different fixatives on 2×2×2 mm biopsies from juvenile pig rib cartilage (including perichondrium, as well as adjacent fat and muscle tissue): neutral buffered formalin, Schaffer's ethanol formalin solution (Schaffer, 1918) and Methacarn [a modified version of Carnoy′s mixture containing methanol/acetic acid/chloroform (Puchtler et al., 1970)]. Conventional formalin fixation yielded unsatisfactory results concerning cartilage matrix staining due to three reasons. First, after staining with a positively charged contrast agent such as Ruthenium Red, absolute CT numbers (Hounsfield units) in cartilage matrix were, in most cases, lower in formalin-fixed

Development (2020) 147, dev187633. doi:10.1242/dev.187633

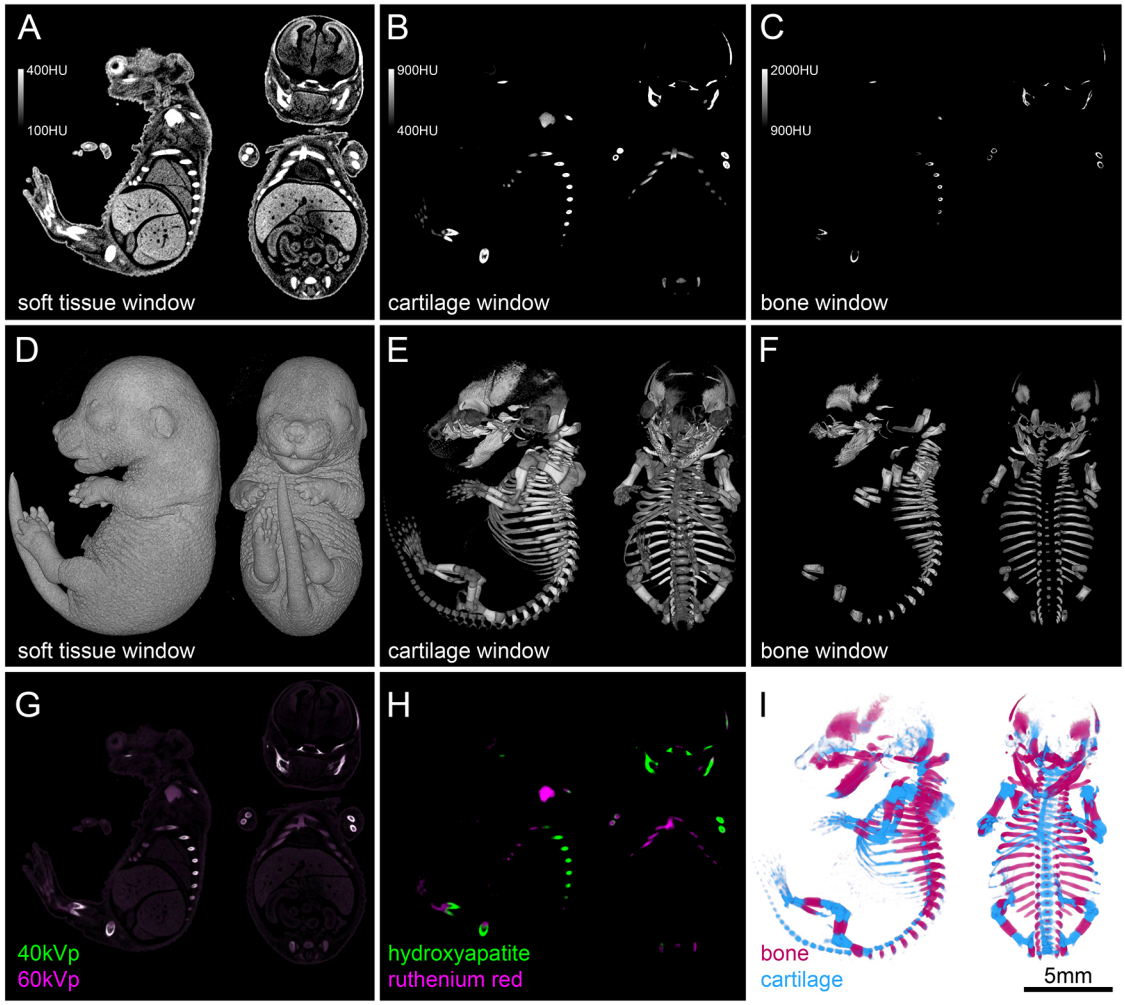

Fig. 3. MicroCT and microDECT imaging of skeletal development in an E16.5 mouse foetus. Analogous to clinical CT, different windowing settings were adapted for the visualisation of soft tissues, cartilage and bone in single energy 60 kVp/133 µA scans of Ruthenium Red stained foetuses. (A) Virtual slices displayed in soft tissue window (100-400HU). (B) Virtual slices displayed in cartilage window (400-900HU). (C) Virtual slices displayed in bone window (900-2000HU). (D) Volume renderings displayed in soft tissue window (100-400HU). (E) Volume renderings displayed in cartilage window (400-900HU). (F) Volume renderings displayed in bone window (900-2000HU). The developed microDECT protocol allowed spectral separation of bone and cartilage based on different attenuation properties of hydroxyapatite and Ruthenium Red. (G) Overlay of 40 kVp/200 µA and 60 kVp/133 µA scan virtual slices showing bone as whitish (similar attenuation in 40 kVp and 60 kVp), and cartilage and soft tissues as pinkish (comparatively higher attenuation in 60 kVp). (H) Extracted material fractions after basis material decomposition. The histogram of the Ruthenium Red fraction was clipped to exclude soft tissues and specifically show cartilage. (I) Two-channel volume rendering of bone and cartilage based on microDECT scan. The two colourmaps were chosen to closely resemble colours of the traditional clearing and staining method (bone, Alizarin Red; cartilage, Alcian Blue).

specimens when compared with other fixation methods. Second, background staining in perichondrium and muscles was higher in formalin-fixed specimens, thus resulting in an even lower cartilage matrix contrast against surrounding tissues. Third, penetration of the contrast agent solutions was no problem in 2×2×2 mm cartilage biopsies of formalin-fixed material, but in the case of formalin-fixed E16.5 mouse foetuses the Ruthenium Red stain failed to penetrate the specimen within a reasonable timeframe. Alcoholic fixatives such as Schaffer's solution or Methacarn yielded a higher staining intensity and a lower staining background than fixation with neutral formalin. After testing different mixtures and components (e.g. methanol/chloroform, methanol/glacial acetic acid and methanol/sulphuric acid) we finally found that neither addition of chloroform nor acidification of the fixatives (see below) improved staining results. Fixation in either 80% ethanol or 80% methanol yielded highest absolute cartilage matrix staining intensity together with very low background staining, and offered excellent sample penetration properties for staining solutions. For further refinement of the staining protocol, we favoured ethanol over methanol owing to its lower toxicity.

Dye penetration and tissue decalcification

In preliminary experiments, we tested several positively charged molecules containing high-Z elements to achieve staining of cartilage matrix proteoglycans, including Alcian Blue (containing copper), Ruthenium Red, and gadolinium chloride. Both Ruthenium Red and gadolinium chloride provided satisfactory tissue penetration and staining intensities in 2×2×2 mm cartilage biopsies. For further development and refinement of the staining procedure, we favoured Ruthenium Red as it also provides excellent contrast in the light microscope. Ruthenium Red has a long history as a contrast agent for cartilage matrix proteoglycans in electron microscopy (e.g. Shepard and Mitchell, 1977; Thyberg, 1977), but so far has only rarely been considered as a contrast agent for

Development (2020) 147, dev187633. doi:10.1242/dev.187633

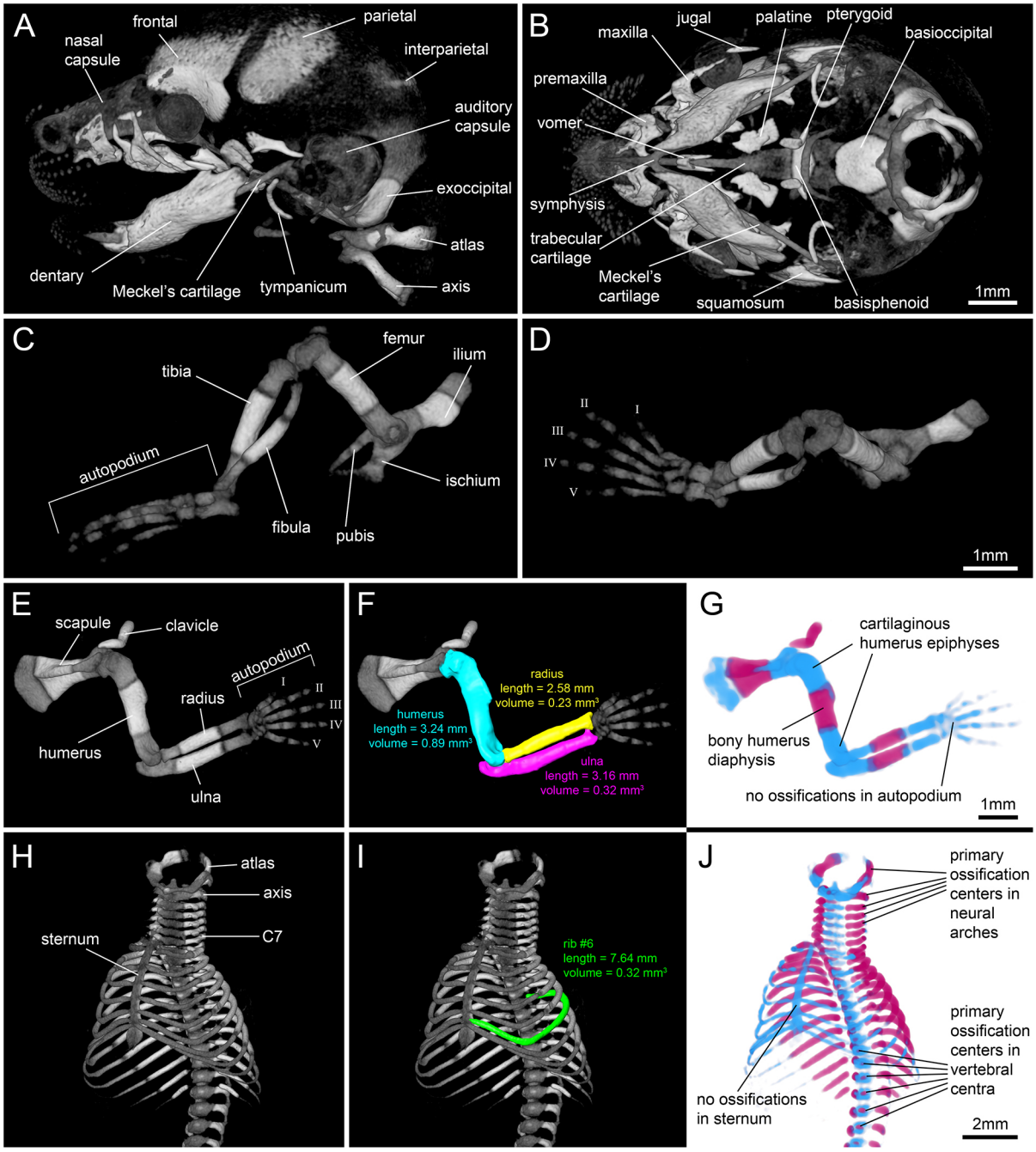

Fig. 4. Higher magnification of cartilage window volume renderings from selected regions of the skeleton of E16.5 mouse foetuses stained with Ruthenium Red. (A) Lateral view of the skull showing dermal bones of the skull (e.g. frontal, parietal and interparietal), ossification centres in the chondrocranium (e.g. exoccipital) and cartilage (e.g. Meckel's cartilage, auditory capsule and nasal capsule). (B) Ventral view of the skull showing the intricate spatial relationships between dermal bones and cartilage (e.g. vomer/trabecular cartilage and dentary/Meckel's cartilage) as well as ossification centres in the cranial base (basioccipital and basisphenoid). (C) Lateral view of the left pelvic girdle and hind limb. (D) Oblique dorsal view of the left pelvic girdle and hind limb (digits labelled with I-V). (E) Lateral view of the right pectoral girdle and forelimb (digits labelled with I-V). (F) Exemplary morphometric measurements taken from humerus, radius and ulna showcase the possible use of the presented method for quantitative evaluation of skeletal development. (G) MicroDECT data of the same forelimb distinctly visualises dermal bones (clavicle) and ossification centres in red, and cartilage in blue. (H) Oblique ventral view of the ribcage showing 13 ribs, of which seven are connected to the sternum. No fused or bifurcating ribs are observed. (I) Morphometric measurements on an exemplary rib. (J) MicroDECT data show the primary ossification centres in vertebrae (neural arches and vertebral centra) and that no ossifications are so far present in the sternum.

microCT imaging (see, for example, Jahn et al., 2018). In preliminary experiments, we used aqueous Ruthenium Red solutions [0.2% (w/v) or 0.1% (w/v) Ruthenium Red in distilled water] in 2×2×2 mm cartilage biopsies, which provided satisfactory cartilage matrix staining intensities. When testing 0.1% aqueous Ruthenium Red in mouse foetuses together with post-staining washing steps in distilled water, we also observed excellent cartilage staining. However, we also noted severe decalcification at dermal and endochondral ossification sites after 48 h of staining (Fig. 6A,B, E-G,K-M). In contrast, we found that staining in 50% ethanol/

Development (2020) 147, dev187633. doi:10.1242/dev.187633

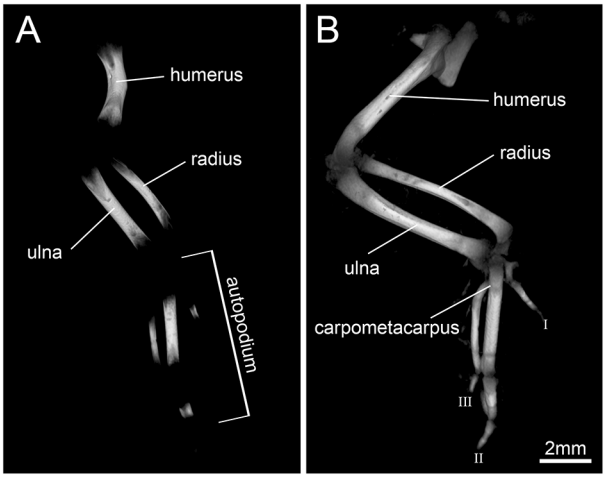

Fig. 5. Application of the Ruthenium Red staining protocol to an E14 chicken embryo wing. (A) Unstained forelimb of an E14 chicken embryo, imaged directly in the fixative (80% ethanol). In the autopodium, one ossification centre can be seen in digit I, two centres in digit II and one centre in digit III. (B) Contralateral wing of the same embryo stained for 72 h with 0.1% (w/v) Ruthenium Red in 50% ethanol. The staining reveals not only the epiphyses of the long bones, but also several skeletal elements of the autopodium that so far show no ossification.

Ruthenium Red together with pre-stain and post-stain washing in 50% ethanol preserved bone mineral very well. We observed no decalcification in volume renderings and virtual slices of foetuses imaged before and after staining (Fig. 6C,D,H-J,N-P). These visual observations were confirmed by length measurements of the diaphyses of humerus, radius, ulna, femur, tibia and fibula (Fig. 6Q,R). Furthermore, scanning of foetuses 4 weeks after mounting showed that bone mineral was preserved in specimens mounted in 1.5% low melt agarose in 40% ethanol. However, we also observed that foetuses stained in 50% ethanol solution and gradually re-hydrated to distilled water showed decalcification starting at 30% ethanol solution and continuing at lower alcohol concentrations. Taken together, these findings suggest that the Ruthenium Red staining procedure modifies bone mineral, but the mineral is not soluble in 50% and 40% ethanol, and therefore stays in place, resulting in no observable mineral loss in the microCT images.

Fixation and staining in an acidic environment

While developing the presented protocol, we tested several acidic fixatives and staining solutions. We initially followed the tradition of clearing and staining approaches, where the cartilage stain Alcian Blue is applied in a highly acidic environment (Hanken and Wassersug, 1981), making it specific for sulphated matrix proteoglycans. We tested analogue procedures also for Ruthenium Red staining. When using 0.2% (w/v) aqueous Ruthenium Red at pH 2.5 to stain 2×2×2 mm biopsies of rib cartilage, the staining pattern was highly specific for cartilage matrix, but retention of the dye was significantly lower when compared with staining with 0.2% (w/v) aqueous Ruthenium Red at pH 5.4. Similarly, post-fixation of formalin-fixed samples of an E16.5 mouse foetal ribcage with either methanol/chloroform/sulphuric acid (pH 1.6) or methanol/chloroform/glacial acetic acid/sulphuric acid (pH 1.4) and subsequent staining with aqueous Ruthenium Red resulted in a highly specific cartilage staining pattern. We found that, macroscopically, the ribs stained deep red, while the skin, muscles and connective tissue remained whitish/colourless (data not shown). Although this staining result was perfect for stereomicroscopic evaluation, we found that this highly specific staining pattern resulted in very low X-ray attenuation in the cartilage matrix, making cartilage indistinguishable from surrounding tissues in reconstructed microCT volumes. Taken together, these data suggest that over-staining of the sample with a positively charged contrast agent at rather neutral pH levels is necessary to obtain reasonably high X-ray attenuation in cartilage matrix, although background staining is also slightly intensified (Figs 1E and 2B,C).

Important technical issues and possible pitfalls

The whole specimen preparation protocol is simple and reproducible. Minor variations in absolute staining intensities occur. Several technical issues that seem to be crucial should be highlighted. Common to all procedures where diffusion plays a role, temperature is critical. Staining E16.5 mouse foetuses for 48 h at 25-27°C resulted in a homogeneous staining pattern. However, if the lab temperature was lower (20-22°C), Ruthenium Red did not penetrate the whole specimen within 48 h. We also found that shaking the samples on a rocker table was critical to ensure the staining of E16.5 mouse foetuses within 48 h. Another important note concerns the Ruthenium Red staining solution, which has to be freshly prepared as follows: first, a 0.2% (w/v) aqueous Ruthenium Red solution is prepared by dissolving Ruthenium Red powder in distilled water, using a magnetic stirrer (this solution may be stored at 4°C for several days). For use, an equal part of absolute ethanol is slowly added to this aqueous stock solution while stirring constantly on a magnetic agitator. This 50% ethanol solution should be immediately used. We found that filtration of the Ruthenium Red solution is not necessary, if the solution is constantly stirred for at least 1 h.

Evaluation, validation and future refinements of the presented workflow

Tissue shrinkage

In previous microCT studies using X-ray dense contrast agents, shrinkage has been a commonly reported problem (Heimel et al., 2019; Schmidt et al., 2010; Vickerton et al., 2013), and it has been shown that hydrogel embedding before iodine staining avoids staining-induced shrinkage artefacts in developmental phenotyping (Wong et al., 2013). In the present workflow, no shrinkage was observed during the staining step, and the foetuses had the same size before and after staining (Fig. 1B,C). In fact, the total volume of foetuses after staining (including a partial re-hydration to 50% ethanol) was even slightly higher when compared with the volume of foetuses after fixation in 80% ethanol. This indicates that in the whole workflow, shrinkage effects are primarily caused by ethanol dehydration. However, more careful and detailed evaluation of shrinkage effects are needed at all steps of the workflow before the presented technique is ready to use for large-scale quantitative evaluations of skeletal development.

Decalcification

Visual evaluation of E16.5 mouse foetuses, as well as length measurements of ossification centres, suggest that no decalcification occurs when staining specimens in 50% ethanol solution (Fig. 6). However, these findings need validation by analytical chemistry. For example, calcium concentrations in staining and washing solutions could be measured by means of inductively coupled plasma optical emission spectrometry (ICP-OES) (Chow et al., 2019) to evaluate the extent of bone mineral loss during staining and washing steps. This would be particularly important for quantitative studies on bone mineral density during development (Percival et al., 2014).

Development (2020) 147, dev187633. doi:10.1242/dev.187633

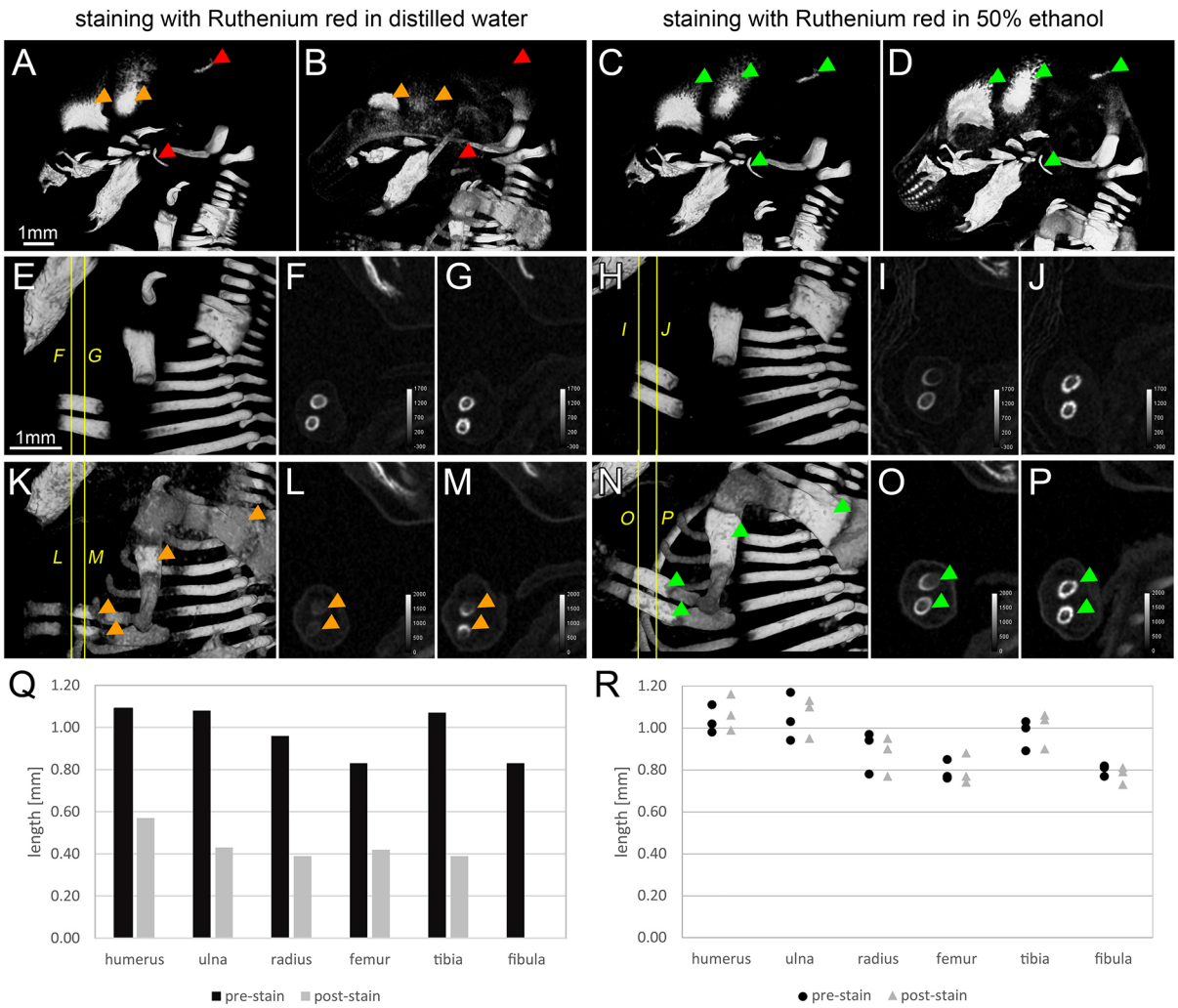

Fig. 6. Comparison of Ruthenium Red staining in aqueous solution versus 50% ethanol solution. Staining for 48 h in aqueous solution and washing with distilled water results in severe decalcification. In contrast, staining in 50% ethanol solution and subsequent ethanol washing preserves bone mineral. (A) Volume rendering of a skull of an E16.5 mouse foetus before staining. (B) The same specimen as shown in A after staining in aqueous Ruthenium Red solution and washing with distilled water. Red arrowheads indicate some bones that became completely decalcified during the staining procedure, such as the interparietal and the tympanicum (for bone labels, see Fig. 4). Orange arrowheads indicate bones that are partially decalcified during the staining procedure, such as the frontal and parietal (for bone labels, see Fig. 4). (C) Volume rendering of a skull of an E16.5 mouse foetus before staining. (D) The same specimen as shown in C after staining in 50% ethanol Ruthenium Red solution and ethanol washing steps. All bone elements are preserved without any macroscopic signs of decalcification (green arrowheads). (E) Volume rendering of a forelimb of an E16.5 mouse foetus before staining. (F,G) Virtual slices through radius and ulna of the forelimb as shown in E before staining. (K) Volume rendering of the same forelimb shown in E after staining in aqueous Ruthenium Red solution and washing with distilled water. (L,M) Virtual slices through radius and ulna after staining in aqueous Ruthenium Red solution and washing with distilled water. The partial decalcification of scapula, humerus, radius and ulna is indicated by orange arrowheads. (H) Volume rendering of a forelimb of an E16.5 mouse foetus before staining. (I,J) Virtual slices through radius and ulna of the forelimb as shown in H before staining. (N) Volume rendering of the same forelimb shown in H after staining in 50% ethanol Ruthenium Red solution and ethanol washing steps. (O,P) Virtual slices through radius and ulna after staining in 50% ethanol Ruthenium Red solution and ethanol washing steps. No calcification was observed in the scapula, humerus, radius and ulna (green arrowheads). (Q) Measurements of length of limb bone ossifications before and after staining with aqueous Ruthenium Red solution clearly show that decalcification in these elements results in a shorter length of the ossified diaphyses (n=1 foetus). (R) Measurement of length of limb bone ossifications before and after staining with 50% ethanol Ruthenium Red solution show that size of these diaphyses did not change during staining (n=3 foetuses).

Future refinements of the workflow

The presented workflow allows, for the first time, high-contrast imaging of the complete E16.5 mouse skeleton using X-ray microCT. We surmise that the presented protocol may be improved with regard to several issues, mainly concerning dual energy imaging protocols. In our currently available setup, 40 kVp was the lowest source voltage accessible for imaging. By applying a 0.1 mm molybdenum filter, we managed to obtain a suitable spectrum for Ruthenium Red imaging. However, this filtering heavily reduced photon flux. Consequently, we had to use a long acquisition time and we needed to resample the two energy volumes by twofold prior to basis material decomposition. Furthermore, we had to use several image filtering steps for denoising, resulting in a decrease in image quality and a loss of minute skeletal structures, such as the interparietal, during the basis material decomposition step (see comparison of Fig. 3E,I). Arguably, a 30 kVp/60 kVp energy pair would be more efficient for the separation of Ruthenium Red and bone mineral. Hence, the presented data serve as a proof of principle that two-channel imaging of bone and cartilage is feasible with lab-based scanners. MicroDECT image quality and resolution are amenable to substantial improvement in future studies.

Development (2020) 147, dev187633. doi:10.1242/dev.187633

Furthermore, synchrotron sources allow imaging with monochromatic X-rays, which makes separation of materials even more effective.

Concerning the range of possible samples, we demonstrated that the presented cartilage staining protocol works for E16.5 mice and E14 chicken limbs. Owing to the much larger size of the E14 chicken embryos, we intentionally chose to stain only their limbs, because the E14 chicken limbs and the E16.5 mouse foetuses are of a similar size. We thus expected that the developed staining protocol would work well with minor modifications. Future methodological refinements are necessary to adapt the presented workflow to a larger range of samples. In the next step, it is therefore essential to adapt the staining protocol to earlier and later time points in mouse development, in order to study developmental series, as shown for the cartilaginous cranial base by McBratney-Owen et al. (2008). Arguably, larger foetuses and newborn mice will require longer staining times, and potentially some further pre-treatment to make the specimen fully permeable to the contrast agent. Pre-treatment strategies may include removing of the skin of newborn mice (Rigueur and Lyons, 2014) and/or chemical treatment with some permeabilisation agent, such as acetone (Falke et al., 2020; Rigueur and Lyons, 2014).

Limitations

Scan resolution and Field of View (FOV)

In this work, we imaged entire E16.5 foetuses in single scans with a FOV of 18.0 mm and an isotropic voxel size of 8.77 µm. This scan resolution allows both the visual phenotyping of the gross skeletal features, and the extraction of quantitative data for larger skeletal elements (Fig. 4). However, at 8.77 µm voxel size microCT volumes may fail to depict finest skeletal detail or tiny bony elements that could be detected by cleared and stained specimens or histological sections. This limitation in scan resolution is not an inherent technical limitation of microCT imaging, but is dependent on the required FOV and the pixel resolution of the X-ray detector assembly. Thus, if minute skeletal elements were the focus of an investigation, higher resolution interior tomographies of the specific region of interest (ROI) with voxel sizes down to 1 µm or even below would be required. Alternatively, microCT investigations may be correlated to findings from histology for revealing fine skeletal details (Figs S1 and S2).

Discrimination of bone and calcified cartilage

The presented microDECT imaging protocol allows the unambiguous spectral separation of calcium and ruthenium. However, calcium mineral in calcified cartilage cannot be spectrally separated from calcium mineral in bone. Therefore, the extracted hydroxyapatite fraction (Fig. 3H) does not contain exclusively bone, but also calcified cartilage matrix occurring in primary ossification centres (POCs) during endochondral ossification (Figs S1 and S2). Despite the inaccuracy of terming all observed mineralisations as ‘bone’ [including POCs of long bones and other endochondral ossifications sites (e.g. in the skull or vertebrae)], we think that this terminological simplification is acceptable in the present context of imaging the entire E16.5 mouse skeleton. Furthermore, the 3D renderings predominantly show the bone collar of long bones, while the calcified cartilage matrix of each POC is mostly hidden inside the bone collar (Figs S1 and S2). This would be different in secondary ossification centres (SOCs), where calcified cartilage is not surrounded by perichondral ossification. However, at E16.5 of mouse development, no SOCs are present. Taken together, bone and calcified cartilage cannot be separated based on their spectral properties, but they could be separated in high-resolution microCT images by using morphological characteristics in correlation with histology (Figs S1 and S2).

Applicability to natural history museum collections

For two main reasons, the presented workflow may have limited applicability for collection material. The first reason concerns fixation. Our experiments showed that formalin fixation yields unsatisfactory staining of cartilage with the present protocol. As such, formalin-fixed specimen collections are not accessible. However, some museum collections also contain ethanol-preserved specimens, which could be processed and imaged. The second reason concerns the potential modification of samples during the staining procedure, which would not be compatible with the requirements of most specimen collections. Currently, we do not know whether the presented staining procedure is fully reversible without causing adverse and permanent changes in the samples.

Possible applications

The workflow presented here provides 3D information on developing cartilage, thus fostering both the qualitative visual assessment of the developing skeleton (Figs 3, 4 and 5) as well as quantitative measurements on skeletal elements (Fig. 4F,I). As such, it represents a first step towards fully automated 3D analysis of skeletal development. Genuine 3D data of skeletal development are highly valuable for different areas of research. Most importantly, the presented workflow allows skeletal phenotyping for screening of developmental disorders, as well as the quantitative characterisation of developmental malformations. It may be used in both phenotyping of genetically modified mouse models (such as knockout mutants) and the study of developmental toxicity effects of test agents. As an example, past investigations in these fields frequently evaluated the limbs and ribcage of embryos and foetuses (Bird et al., 2018; White et al., 2003). At the presented image quality in single energy microCT scans of E16.5 mouse foetuses (scanning at 60 kVp/133 µA, voxel size of 8.77 µm), developmental disorders such as fusion of vertebrae or ribs, or bifurcation of ribs could be easily detected. Another potential application of the presented method lies in the field of evo-devo (Mitteröcker, 2020; Müller, 2007), which also significantly benefits from the quantitative characterisation of developmental processes.

Outlook

Quantitative phenotyping of the developing skeleton based on microCT images has the potential for high-throughput analyses. With lab-based setups, scan acquisition time is typically in the range of one to several hours, depending on system configuration and X-ray detector, thus 10-100 specimens may be imaged per week when using single energy 60 keV/133 µA scans at an image quality similar to the images shown here. With synchrotron X-ray imaging beamlines, acquisition times are shortened to minutes (Carlton et al., 2016; Rousseau et al., 2015) or seconds (Maire and Withers, 2014) per specimen, thus potentially allowing the imaging of several hundreds of specimens per day. The cartilage contrast achieved with Ruthenium Red staining allows intensity-based image segmentation of many skeletal elements, e.g. the long bones of limbs, providing a basis for automated pipelines for quantitative morphometric evaluation. Thus, we propose the presented workflow as a promising alternative to established methods for the phenotyping of vertebrate skeletal development that should be valuable for various research fields within the life sciences.

MATERIALS AND METHODS

Sample preparation

Animal husbandry and harvesting of E16.5 C57BL/6 wild-type mouse foetuses

Animals were bred in house and kept specific pathogen free according to FELASA recommendations (Mähler Convenor et al., 2014) and under

Development (2020) 147, dev187633. doi:10.1242/dev.187633

controlled environmental conditions (temperature 22±1°C, relative humidity of 40–60%) in a facility for laboratory rodents. Food (mouse maintenance diet, sterilized, V1534-727 or mouse breeding diet, sterilized, V1124-727, ssniff Spezialdiäten, Soest, Germany) and water were provided *ad libitum*. Mice were maintained in individually ventilated cages (Type IIL, Tecniplast, Buguggiate, Italy) lined with bedding material (Safe Select, heat treated, S-SELECT-09322, J. Rettenmaier und Soehne, Rosenberg, Germany) and enriched with nesting material (Pur-Zellin 4×5 cm, 1432530; Paul Hartmann, Wiener Neudorf, Austria). For harvesting embryonic day (E)16.5 foetuses, mice were mated in the afternoon and female mice were checked for vaginal plugs the next morning and separated from the stud male. At E16.5 females were euthanized by cervical dislocation and foetuses were harvested and rinsed in phosphate-buffered saline. Experimental procedures were discussed and approved by the institutional ethics and animal welfare committee in accordance with good scientific practice guidelines and national legislation (animal breeding licence number: BMWFW-68.205/0049-WF/V/3b/2015).

Fixation and staining of E16.5 mouse foetuses

E16.5 C57BL/6 wild-type mouse foetuses (stage 24 of Theiler, 1989) were fixed in 80% ethanol at 4°C for 7 days. During fixation, a maximum of three mouse foetuses were kept in 50 ml fixative. All subsequent steps (i.e. pre- and post-staining washing steps as well as staining itself) were carried out in 25 ml medium in a horizontally oriented 50 ml centrifuge tube (one specimen per tube) at 25°C, using gentle horizontal shaking. After fixation, the foetuses were washed twice in 50% ethanol (2 h per washing step). Staining was carried out for 48 h in 0.1% (w/v) Ruthenium Red (Sigma Aldrich, 00541-1G) in 50% ethanol. After staining, foetuses were gently blotted with paper tissue and washed for 2 h in 50% ethanol. During this first washing step, a lot of unbound Ruthenium Red was rinsed out of the specimens, colouring the washing medium pink. Next, foetuses were washed overnight (16 h) in 50% ethanol followed by two washing steps (2 h per step) in 40% ethanol. Before the last washing step, most unbound Ruthenium Red was already washed out of the samples, so the last washing medium showed almost no pink coloration. Finally, the foetuses were mounted in 1.5% low melt Agarose (Carl Roth, 6351.5) in 40% ethanol in 5 ml polypropylene tubes. The whole sample preparation workflow is graphically summarised in Fig. 1A.

Fixation and staining of E14 chicken embryos

E14 chicken embryos (stage 40 of Hamburger and Hamilton, 1951) were harvested from White E.P. SPF eggs (VALO BioMedia, Osterholz-Scharmbeck, Germany) and fixed in 80% ethanol at 4°C for 7 days. During fixation, each single specimen was placed in a 100 ml sample container and the fixative was replaced after 3 days. Subsequently, a forelimb was collected and processed as described above for the mouse foetuses. The only difference was a slightly longer Ruthenium Red staining time of 72 h to compensate for the larger specimen size.

X-ray microCT and microDECT imaging

All specimens shown in this study were imaged using an XRadia MicroXCT-400 (Carl Zeiss X-Ray Microscopy). Sample containers (5 ml polypropylene tubes containing the agarose-embedded specimens, Fig. 1D) were glued to the sample stage with a double-sided adhesive tape and imaged using the 0.4× detector assembly over a 360° sample rotation (Fig. 1F).

MicroCT imaging of E16.5 mouse foetuses

E16.5 mouse foetuses were imaged using a 60 kVp/133 µA X-ray spectrum filtered by the Zeiss LE#2 filter. Projection images were recorded with 30 s exposure time (camera binning=1) per projection and an angular increment of 0.225° between projections. Tomographic sections were reconstructed using the XMReconstructor software supplied with the scanner. Isotropic voxel size in the reconstructed volumes was 8.77 µm. Reconstructed volumes were exported in *.TXM format.

MicroCT imaging of E14 chicken embryo forelimbs

E14 chicken embryo forelimbs were imaged using a 60 kVp/133 µA X-ray spectrum filtered by the Zeiss LE#2 filter. Projection images were recorded with 10 s exposure time (camera binning=1) per projection and an angular increment of 0.225° between projections. Tomographic sections were reconstructed using the XMReconstructor software supplied with the scanner. Isotropic voxel size in the reconstructed volumes was 12.01 µm. Reconstructed volumes were exported in *.TXM format.

Microscopic dual energy imaging of an E16.5 mouse foetus

In addition to conventional microCT scans, we acquired a microscopic dual energy CT (microDECT) scan from one mouse foetus. The energy pair used was 40 kVp/200 µA filtered by a 0.1 mm Molybdenum filter (lower energy scan, exposure time=100 s, angular increment=0.225°) and 60 kVp/133 µA filtered by the Zeiss LE#2 filter (higher energy scan, exposure time=30 s, angular increment=0.225°). This energy pair allowed separating spectral signals from bone mineral (hydroxyapatite) and Ruthenium Red stained tissue. The K-edge of ruthenium is at 22.1 keV; thus, the higher energy scan shows stronger ruthenium attenuation relative to bone mineral attenuation in comparison with the lower energy scan. For details on the dual energy imaging workflow see Handschuh et al. (2017). Reconstructed volumes were exported in *.TXM format.

Image processing and data visualisation

Conventional 60 kVp/133 µA microCT scans

MicroCT scans were imported into the commercial 3D reconstruction software package Amira 2019.1 (FEI SAS; part of ThermoFisher Scientific). Volumes were filtered with a 3D bilateral filter and a 3D Gaussian filter to increase signal-to-noise ratio. Image intensities were standardised to Hounsfield units (HU) based on measurement of a water-air phantom (Handschuh et al., 2017). For visualization of the staining results in the 60 kVp scans of mouse foetuses we used virtual slices and volume renderings using different histogram settings in analogy to windowing in clinical computed tomography (soft tissue window, 100-400 HU; cartilage window, 400-900 HU; bone window, 900-2000 HU). For displaying selected parts of the foetal mouse skeleton, such as the skull, forelimb, hind limb and ribcage, we used the Amira volume segmentation tool Volume edit to crop selected body regions.

Microscopic dual energy CT scans

Processing of the dual energy scans, image registration and basis material decomposition were carried out as described previously (Handschuh et al., 2017). In brief, the two scans were imported into Amira 2019.1, converted to Hounsfield units (HUs), filtered using a 3D bilateral filter and registered based on the normalised mutual information. The registered volumes were resampled by a factor of 2 and further filtered using a 3D median and a 3D Gaussian filter, mainly to compensate for the comparatively higher level of image noise in the 40 kVp scan. Subsequently, three material fractions (hydroxyapatite, Ruthenium Red and agarose in 40% ethanol) were extracted from the two scanning energies (Badea et al., 2012; Handschuh et al., 2017) using a custom MATLAB (The Mathworks) program, which is publically available on Github (https://github.com/microDECT/DECTDec). The extracted hydroxyapatite and ruthenium fractions were visualised both as colour overlays on virtual slices and as two-channel 3D volume renderings. The colourmaps for volume rendering were adjusted to closely resemble the colours of traditionally cleared and stained specimens (bone, red; cartilage, blue).

Exemplary morphometric measurements on stained skeletal elements

MicroCT datasets are inherently isotropic in 3D and can be used for a variety of morphometric measurements. To showcase possible quantitative applications, the humerus, radius, ulna and one rib from a 60 kVp scan of an E16.5 mouse foetus were segmented semi-automatically (intensity-based segmentation followed by manual separation of skeletal elements). Based on these segmentations, surface models were created and the volume of segmented structures was measured using the Amira tool Surface Area Volume. For humerus, radius and ulna, the linear length was measured based on the first principal axis of the respective surface (after re-orienting the surface with the tool Align Principal Axis). For the rib, a skeleton spatial

graph was calculated (tool Centreline Tree, number of parts=1), the spatial graph was smoothed (tool Smooth Line Set, 100 iterations) and finally the length of the skeleton line was measured (tool Spatial Graph Statistics).

Acknowledgements
We thank the University Clinic for Poultry and Fish Medicine of the University of Veterinary Medicine Vienna for providing chicken embryos. We also thank Brigitte Machac for performing histological sectioning and staining (Figs S1 and S2) and Stefan Kummer for help with acquiring stereomicroscope images (Fig. 1E) of the cut mouse foetus. This research was supported using resources of the VetCore Facility (Imaging) of the University of Veterinary Medicine Vienna.

Competing interests
The authors declare no competing or financial interests.

Author contributions
Conceptualization: S.G., P.B., S.H.; Methodology: S.G., S.H.; Investigation: S.G., D.F., S.H.; Resources: D.F.; Writing - original draft: S.H.; Writing - review & editing: S.G., P.B., D.F., M.G.; Visualization: S.H.; Supervision: P.B.; Project administration: S.G., P.B., M.G., S.H.

Funding
This research received no specific grant from any funding agency in the public, commercial or not-for-profit sectors.

Supplementary information
Supplementary information available online at
http://dev.biologists.org/lookup/doi/10.1242/dev.187633.supplemental

References
Adams, D., Baldock, R., Bhattacharya, S., Copp, A. J., Dickinson, M., Greene, N. D. E., Henkelman, M., Justice, M., Mohun, T., Murray, S. A. et al. (2013). Bloomsbury report on mouse embryo phenotyping: recommendations from the IMPC workshop on embryonic lethal screening (vol 6, pg 571, 2013). *Dis. Model. Mech.* **6**, 1049-1049. doi:10.1242/dmm.012898

Badea, C. T., Guo, X., Clark, D., Johnston, S. M., Marshall, C. D. and Piantadosi, C. A. (2012). Dual-energy micro-CT of the rodent lung. *Am. J. Physiol. Lung C* **302**, L1088-L1097. doi:10.1152/ajplung.00359.2011

Bird, I. M., Kim, S. H., Schweppe, D. K., Caetano-Lopes, J., Robling, A. G., Charles, J. F., Gygi, S. P., Warman, M. L. and Smits, P. J. (2018). The skeletal phenotype of achondrogenesis type 1A is caused exclusively by cartilage defects. *Development* **145**, dev156588. doi:10.1242/dev.156588

Bouxsein, M. L., Boyd, S. K., Christiansen, B. A., Guldberg, R. E., Jepsen, K. J. and Müller, R. (2010). Guidelines for assessment of bone microstructure in rodents using micro-computed tomography. *J. Bone Miner. Res.* **25**, 1468-1486. doi:10.1002/jbmr.141

Brunt, L. H., Norton, J. L., Bright, J. A., Rayfield, E. J. and Hammond, C. L. (2015). Finite element modelling predicts changes in joint shape and cell behaviour due to loss of muscle strain in jaw development. *J. Biomech.* **48**, 3112-3122. doi:10.1016/j.jbiomech.2015.07.017

Busse, M., Müller, M., Kimm, M. A., Ferstl, S., Allner, S., Achterhold, K., Herzen, J. and Pfeiffer, F. (2018). Three-dimensional virtual histology enabled through cytoplasm-specific X-ray stain for microscopic and nanoscopic computed tomography. *Proc. Natl. Acad. Sci. USA* **115**, 2293-2298. doi:10.1073/pnas.1720862115

Capellini, T. D., Handschuh, K., Quintana, L., Ferretti, E., Di Giacomo, G., Fantini, S., Vaccari, G., Clarke, S. L., Wenger, A. M., Bejerano, G. et al. (2011). Control of pelvic girdle development by genes of the Pbx family and Emx2. *Dev. Dyn.* **240**, 1173-1189. doi:10.1002/dvdy.22617

Carlton, H. D., Elmer, J. W., Li, Y., Pacheco, M., Goyal, D., Parkinson, D. Y. and MacDowell, A. A. (2016). Using synchrotron radiation microtomography to investigate multi-scale three-dimensional microelectronic packages. *J. Vis. Exp.* doi:10.3791/53683

Chandaria, V. V., McGinty, J. and Nowlan, N. C. (2016). Characterising the effects of in vitro mechanical stimulation on morphogenesis of developing limb explants. *J. Biomech.* **49**, 3635-3642. doi:10.1016/j.jbiomech.2016.09.029

Chow, D. H., Zheng, L., Tian, L., Ho, K.-S., Qin, L. and Guo, X. (2019). Application of ultrasound accelerates the decalcification process of bone matrix without affecting histological and immunohistochemical analysis. *J. Orthop. Translat.* **17**, 112-120. doi:10.1016/j.jot.2018.08.001

Cockman, M. D., Blanton, C. A., Chmielewski, P. A., Dong, L., Dufresne, T. E., Hookfin, E. B., Karb, M. J., Liu, S. and Wehmeyer, K. R. (2006). Quantitative imaging of proteoglycan in cartilage using a gadolinium probe and microCT. *Osteoarthr Cartilage* **14**, 210-214. doi:10.1016/j.joca.2005.08.010

Das Neves Borges, P., Forte, A. E., Vincent, T. L., Dini, D. and Marenzana, M. (2014). Rapid, automated imaging of mouse articular cartilage by microCT for early detection of osteoarthritis and finite element modelling of joint mechanics. *Osteoarthr Cartilage* **22**, 1419-1428. doi:10.1016/j.joca.2014.07.014

de Bournonville, S., Vangrunderbeeck, S. and Kerckhofs, G. (2019). Contrast-enhanced MicroCT for virtual 3D anatomical pathology of biological tissues: a literature review. *Contrast Media Mol. Imaging* **2019**, 8617406. doi:10.1155/2019/8617406

Dickinson, M. E., Flenniken, A. M., Ji, X., Teboul, L., Wong, M. D., White, J. K., Meehan, T. F., Weninger, W. J., Westerberg, H., Adissu, H. et al. (2016). High-throughput discovery of novel developmental phenotypes. *Nature* **537**, 508-514. doi:10.1038/nature19356

Dingerkus, G. and Uhler, L. D. (1977). Enzyme clearing of alcian blue stained whole small vertebrates for demonstration of cartilage. *Stain Technol.* **52**, 229-232. doi:10.3109/10520297709116780

Falke, L. L., He, N., Chuva de Sousa Lopes, S. M., Broekhuizen, R., Lyons, K., Nguyen, T. Q. and Goldschmeding, R. (2020). FoxD1-driven CCN2 deletion causes axial skeletal deformities, pulmonary hypoplasia, and neonatal asphyctic death. *J. Cell Commun. Signal* (in press). doi:10.1007/s12079-020-00549-4

Greenbaum, A., Chan, K. Y., Dobreva, T., Brown, D., Balani, D. H., Boyce, R., Kronenberg, H. M., McBride, H. J. and Gradinaru, V. (2017). Bone CLARITY: Clearing, imaging, and computational analysis of osteoprogenitors within intact bone marrow. *Sci. Transl. Med.* **9**, eaah6518. doi:10.1126/scitranslmed.aah6518

Hamburger, V. and Hamilton, H. L. (1951). A series of normal stages in the development of the chick embryo. *J. Morphol.* **88**, 49. doi:10.1002/jmor.1050880104

Handschuh, S., Beisser, C. J., Ruthensteiner, B. and Metscher, B. D. (2017). Microscopic dual-energy CT (microDECT): a flexible tool for multichannel ex vivo 3D imaging of biological specimens. *J. Microsc-Oxford* **267**, 3-26. doi:10.1111/jmi.12543

Hanken, J. and Wassersug, R. (1981). The visible skeleton: a new double-stain technique reveals the nature of the hard tissues. *Funct. Photogr.* **16**, 22-26.

Heimel, P., Swiadek, N. V., Slezak, P., Kerbl, M., Schneider, C., Nurnberger, S., Redl, H., Teuschl, A. H. and Hercher, D. (2019). Iodine-enhanced Micro-CT imaging of soft tissue on the example of peripheral nerve regeneration. *Contrast Media Mol. Imaging* **2019**, 7483745. doi:10.1155/2019/7483745

Jahn, H., Oliveira, I. D., Gross, V., Martin, C., Hipp, A., Mayer, G. and Hammel, J. U. (2018). Evaluation of contrasting techniques for X-ray imaging of velvet worms (Onychophora). *J. Microsc-Oxford* **270**, 343-358. doi:10.1111/jmi.12688

Jing, D., Zhang, S., Luo, W., Gao, X., Men, Y., Ma, C., Liu, X., Yi, Y., Bugde, A., Zhou, B. O. et al. (2018). Tissue clearing of both hard and soft tissue organs with the PEGASOS method. *Cell Res.* **28**, 803-818. doi:10.1038/s41422-018-0049-z

Johnson, J. T., Hansen, M. S., Wu, I., Healy, L. J., Johnson, C. R., Jones, G. M., Capecchi, M. R. and Keller, C. (2006). Virtual histology of transgenic mouse embryos for high-throughput phenotyping. *PLoS Genet.* **2**, e61. doi:10.1371/journal.pgen.0020061

Karhula, S. S., Finnilä, M. A., Lammi, M. J., Ylärinne, J. H., Kauppinen, S., Rieppo, L., Pritzker, K. P. H., Nieminen, H. J. and Saarakkala, S. (2017). Effects of articular cartilage constituents on phosphotungstic acid enhanced micro-computed tomography. *PLoS ONE* **12**, e0171075. doi:10.1371/journal.pone.0171075

Kaucka, M., Petersen, J., Tesarova, M., Szarowska, B., Kastriti, M. E., Xie, M., Kicheva, A., Annusver, K., Kasper, M., Symmons, O. et al. (2018). Signals from the brain and olfactory epithelium control shaping of the mammalian nasal capsule cartilage. *Elife* **7**, e34465. doi:10.7554/eLife.34465.028

Kerckhofs, G., Sainz, J., Wevers, M., Van de Putte, T. and Schrooten, J. (2013). Contrast-enhanced nanofocus computed tomography images the cartilage subtissue architecture in three dimensions. *Eur. Cells Mater* **25**, 179-189. doi:10.22203/eCM.v025a13

Lecanda, F., Warlow, P. M., Sheikh, S., Furlan, F., Steinberg, T. H. and Civitelli, R. (2000). Connexin43 deficiency causes delayed ossification, craniofacial abnormalities, and osteoblast dysfunction. *J. Cell Biol.* **151**, 931-943. doi:10.1083/jcb.151.4.931

Li, Q. T., Lu, Q. X., Hwang, J. Y., Buscher, D., Lee, K.-F., Izpisua-Belmonte, J. C. and Verma, I. M. (1999). IKK1-deficient mice exhibit abnormal development of skin and skeleton. *Gene Dev.* **13**, 1322-1328. doi:10.1101/gad.13.10.1322

Lukas, P. and Olsson, L. (2018). Sequence and timing of early cranial skeletal development in *Xenopus laevis*. *J. Morphol.* **279**, 62-74. doi:10.1002/jmor.20754

Mähler Convenor, M., Berard, M., Feinstein, R., Gallagher, A., Illgen-Wilcke, B., Pritchett-Corning, K. and Raspa, M. (2014). FELASA recommendations for the health monitoring of mouse, rat, hamster, guinea pig and rabbit colonies in breeding and experimental units. *Lab. Anim.* **48**, 178-192. doi:10.1177/0023677213516312

Maire, E. and Withers, P. J. (2014). Quantitative X-ray tomography. *Int. Mater. Rev.* **59**, 1-43. doi:10.1179/1743280413Y.0000000023

Martins de Souza, E. Silva, J., Utsch, J., Kimm, M. A., Allner, S., Epple, M. F., Achterhold, K. and Pfeiffer, F. (2017). Dual-energy micro-CT for quantifying the time-course and staining characteristics of *ex-vivo* animal organs treated with iodine- and gadolinium-based contrast agents. *Sci. Rep.* **7**, 17387. doi:10.1038/s41598-017-17064-z

McBratney-Owen, B., Iseki, S., Bamforth, S. D., Olsen, B. R. and Morriss-Kay, G. M. (2008). Development and tissue origins of the mammalian cranial base. *Dev. Biol.* **322**, 121-132. doi:10.1016/j.ydbio.2008.07.016

Metscher, B. D. (2009). MicroCT for developmental biology: a versatile tool for high-contrast 3D imaging at histological resolutions. *Dev. Dyn.* **238**, 632-640. doi:10.1002/dvdy.21857

Metscher, B. D. and Müller, G. B. (2011). MicroCT for molecular imaging: quantitative visualization of complete three-dimensional distributions of gene products in embryonic limbs. *Dev. Dyn.* **240**, 2301-2308. doi:10.1002/dvdy.22733

Mitteröcker, P. (2020). Morphometrics in Evolutionary Developmental Biology (in press). In *Evolutionary Developmental Biology - A Reference Guide* (ed. L. Nuño de la Rosa and G. B. Müller). Cham: Springer International Publishing.

Mizutani, R. and Suzuki, Y. (2012). X-ray microtomography in biology. *Micron* **43**, 104-115. doi:10.1016/j.micron.2011.10.002

Müller, G. B. (2007). Evo-devo: extending the evolutionary synthesis. *Nat. Rev. Genet.* **8**, 943-949. doi:10.1038/nrg2219

Müller, M., Kimm, M. A., Ferstl, S., Allner, S., Achterhold, K., Herzen, J., Pfeiffer, F. and Busse, M. (2018). Nucleus-specific X-ray stain for 3D virtual histology. *Sci. Rep.* **8**, 17855. doi:10.1038/s41598-018-36067-y

Nieminen, H. J., Ylitalo, T., Karhula, S., Suuronen, J. P., Kauppinen, S., Serimaa, R., Haeggström, E., Pritzker, K. P. H., Valkealahti, M., Lehenkari, P. et al. (2015). Determining collagen distribution in articular cartilage using contrast-enhanced micro-computed tomography. *Osteoarthr Cartilage* **23**, 1613-1621. doi:10.1016/j.joca.2015.05.004

Oest, M. E., Jones, J. C., Hatfield, C. and Prater, M. R. (2008). Micro-CT evaluation of murine fetal skeletal development yields greater morphometric precision over traditional clear-staining methods. *Birth Defects Res. B Dev. Reprod. Toxicol.* **83**, 582-589. doi:10.1002/bdrb.20177

Okumura, M., Ishikawa, A., Aoyama, T., Yamada, S., Uwabe, C., Imai, H., Matsuda, T., Yoneyama, A., Takeda, T. and Takakuwa, T. (2017). Cartilage formation in the pelvic skeleton during the embryonic and early-fetal period. *PLoS ONE* **12**, e0173852.

Pardo-Martin, C., Allalou, A., Medina, J., Eimon, P. M., Wählby, C. and Yanik, M. F. (2013). High-throughput hyperdimensional vertebrate phenotyping. *Nat. Commun.* **4**, 1467. doi:10.1038/ncomms2475

Park, E.-H. and Kim, D. S. (1984). A procedure for staining cartilage and bone of whole vertebrate larvae while rendering all other tissues transparent. *Stain Technol.* **59**, 269-272. doi:10.3109/10520298409113869

Percival, C. J., Huang, Y., Jabs, E. W., Li, R. and Richtsmeier, J. T. (2014). Embryonic craniofacial bone volume and bone mineral density in Fgfr2(+/P253R) and nonmutant mice. *Dev. Dyn.* **243**, 541-551. doi:10.1002/dvdy.24095

Puchtler, H., Waldrop, F. S., Meloan, S. N., Terry, M. S. and Conner, H. M. (1970). Methacarn (Methanol-Carnoy) fixation - practical and theoretical considerations. *Histochemistry* **21**, 97-116. doi:10.1007/BF00306176

Reissig, L. F., Herdina, A. N., Rose, J., Maurer-Gesek, B., Lane, J. L., Prin, F., Wilson, R., Hardman, E., Galli, A., Tudor, C. et al. (2019). The Col4a2$^{em1(IMPC)Wtsi}$ mouse line: lessons from the deciphering the mechanisms of developmental disorders program. *Biol. Open* **8**, bio042895. doi:10.1242/bio.042895

Rigueur, D. and Lyons, K. M. (2014). Whole-mount skeletal staining. *Methods Mol. Biol.* **1130**, 113-121. doi:10.1007/978-1-62703-989-5_9

Rousseau, D., Widiez, T., Di Tommaso, S., Rositi, H., Adrien, J., Maire, E., Langer, M., Olivier, C., Peyrin, F. and Rogowsky, P. (2015). Fast virtual histology using X-ray in-line phase tomography: application to the 3D anatomy of maize developing seeds. *Plant Methods* **11**, 55. doi:10.1186/s13007-015-0098-y

Sakata-Haga, H., Uchishiba, M., Shimada, H., Tsukada, T., Mitani, M., Arikawa, T., Shoji, H. and Hatta, T. (2018). A rapid and nondestructive protocol for whole-mount bone staining of small fish and *Xenopus*. *Sci. Rep.* **8**, 7453. doi:10.1038/s41598-018-25836-4

Schaffer, J. (1918). Veränderungen an Gewebselementen durch einseitige Wirkung der Fixierungsflüssigkeit und Allgemeines über Fixierung. *Anat Anz* **51**, 353-398.

Schmidt, E. J., Parsons, T. E., Jamniczky, H. A., Gitelman, J., Trpkov, C., Boughner, J. C., Logan, C. C., Sensen, C. W. and Hallgrimsson, B. (2010). Micro-computed tomography-based phenotypic approaches in embryology: procedural artifacts on assessments of embryonic craniofacial growth and development. *BMC Dev. Biol.* **10**, 18. doi:10.1186/1471-213X-10-18

Shapiro, F. (1992). Vertebral development of the chick embryo during days 3-19 of incubation. *J. Morphol.* **213**, 317-333. doi:10.1002/jmor.1052130305

Shepard, N. and Mitchell, N. (1977). Localization of articular-cartilage proteoglycan by electron-microscopy. *Anat. Rec.* **187**, 463-475. doi:10.1002/ar.1091870404

Simons, E. V. and van Horn, J. R. (1971). A new procedure for whole-mount alcian blue staining of the cartilaginous skeleton of chicken embryos, adapted to the clearing procedure in potassium hydroxide. *Acta Morphol. Neerl Scand* **8**, 281-292.

Solomon, H. M., Murzyn, S., Rendemonti, J., Chapman, S., Skedzielewski, T., Jucker, B. M., Stanislaus, D. and Alsaid, H. (2018). The use of micro-CT imaging to examine and illustrate fetal skeletal abnormalities in Dutch Belted rabbits and to prove concordance with Alizarin Red stained skeletal examination. *Birth Defects Res.* **110**, 276-298. doi:10.1002/bdr2.1168

Theiler, K. (1989). *The House Mouse: Atlas of Embryonic Development*. New York, USA: Springer-Verlag.

Thyberg, J. (1977). Electron microscopy of cartilage proteoglycans. *Histochem. J.* **9**, 259-266. doi:10.1007/BF01004761

Vickerton, P., Jarvis, J. and Jeffery, N. (2013). Concentration-dependent specimen shrinkage in iodine-enhanced microCT. *J. Anat.* **223**, 185-193. doi:10.1111/joa.12068

Wassersug, R. J. (1976). A procedure for differential staining of cartilage and bone in whole formalin-fixed vertebrates. *Stain Technol.* **51**, 131-134. doi:10.3109/10520297609116684

White, P. H., Farkas, D. R., McFadden, E. E. and Chapman, D. L. (2003). Defective somite patterning in mouse embryos with reduced levels of Tbx6. *Development* **130**, 1681-1690. doi:10.1242/dev.00367

Wong, M. D., Dorr, A. E., Walls, J. R., Lerch, J. P. and Henkelman, R. M. (2012). A novel 3D mouse embryo atlas based on micro-CT. *Development* **139**, 3248-3256. doi:10.1242/dev.082016

Wong, M. D., Spring, S. and Henkelman, R. M. (2013). Structural stabilization of tissue for embryo phenotyping using micro-CT with iodine staining. *PLoS ONE* **8**, e84321. doi:10.1371/journal.pone.0084321

Wong, M. D., Maezawa, Y., Lerch, J. P. and Henkelman, R. M. (2014). Automated pipeline for anatomical phenotyping of mouse embryos using micro-CT. *Development* **141**, 2533-2541. doi:10.1242/dev.107722

Xie, L., Lin, A. S. P., Guldberg, R. E. and Levenston, M. E. (2010). Nondestructive assessment of sGAG content and distribution in normal and degraded rat articular cartilage via EPIC-mu CT. *Osteoarthr Cartilage* **18**, 65-72. doi:10.1016/j.joca.2009.07.014

Xie, L., Lin, A. S. P., Levenston, M. E. and Guldberg, R. E. (2009). Quantitative assessment of articular cartilage morphology via EPIC-mu CT. *Osteoarthr Cartilage* **17**, 313-320. doi:10.1016/j.joca.2008.07.015

Yamazaki, Y., Yuguchi, M., Kubota, S. and Isokawa, K. (2011). Whole-mount bone and cartilage staining of chick embryos with minimal decalcification. *Biotech. Histochem.* **86**, 351-358. doi:10.3109/10520295.2010.506158

Yaryhin, O. and Werneburg, I. (2019). The origin of orbitotemporal diversity in lepidosaurs: insights from tuatara chondrocranial anatomy. *Vertebrate Zool.* **69**, 169-181.